A Partitioned Shared Control Strategy for Interaction-oriented End-effector Tasks using an Orbital Robot

Hrishik Mishra, Ribin Balachandran, Marco De Stefano and Christian Ott

***Abstract*— In this paper, a novel partitioned shared controller is proposed, which exploits a fully-actuated orbital robot to perform a primary end-effector task involving environmental interactions. This task is remotely performed using a bilateral teleoperation controller, while a secondary task is automatically controlled *in situ* for operational safety in a partitioned manner. In particular, the proposed method is derived as a modified 4-Channel teleoperation architecture. The orbital robot's momentum and shape (joints) dynamics are exploited to benefit the controller design. Asymptotic stability and finite-gain L_2-stability are proved in the absence and presence of external interactions, respectively. Furthermore, the proposed method is validated experimentally on a hardware-in-the-loop facility.**

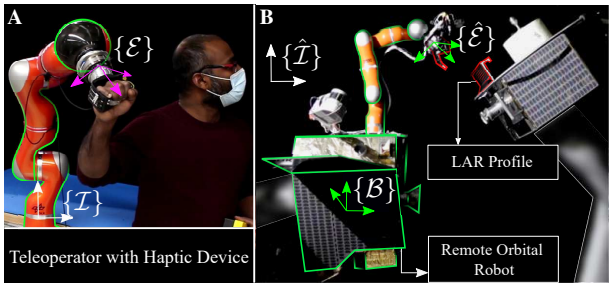

Fig. 1: Teleoperation scenario. **A**: Teleoperator with haptic device; **B**: Remote orbital robot and its environment.

I. Introduction

A key agent in servicing operations in orbit [1] is the orbital robot, which is a manipulator-equipped spacecraft. Control approaches for the orbital robot's end-effector are broadly classified as *free-floating* and *free-flying* [2]. The former precludes spacecraft actuation (thrusters) and uses the reduced orbital robot as an underactuated manipulator [3], while the latter exploits the fully-actuated orbital robot, see [2], [4], [5]. Naturally, *free-floating* approaches offer fuel-efficiency in free motion, however, only *free-flying* approaches enable full motion stabilization, i.e., avoid drifts, during interactions. Thus, it is desirable for a single controller to offer functionalities of both approaches to avoid switching or heuristic blending mechanisms [4].

For the orbital robot, although automatic control [2], [4], [5] is the crowning glory, its technology-readiness for unplanned tasks, e.g. extravehicular tactile inspection, might not be satisfactory [6]. In this case, teleoperated control [6], [7], emerges as a pragmatic approach because it employs the advantage of human intuition for corrective actions. The orbital robot is teleoperated from either an on-orbit neighbouring spacecraft [8] or an on-ground station [9], [10]. A notable difference between these two approaches is that the communication time-delays are negligible in the former, but not in the latter [8]. A Bilateral Teleoperation Controller (BTC) [11]–[13] is an archetypal teleoperation approach, which stabilizes a coordination task error, i.e., the error between the desired motion generated by the human operator using a haptic device and the motion of the remote (orbital) robot. An example of the operational scenario for the BTC is shown in Fig. 1. In this method, the measurements of positions (P) and interaction forces (F) from the two agents are transmitted over communication channels. A BTC-specific performance measure is the *transparency* condition, which requires a dynamically consistent force-matching between the haptic device and the remote (orbital) robot [11]. *Transparency* ensures that the interaction forces between the remote robot and its environment are experienced intuitively by the human teleoperator [12]. To this end, these remotely sensed interaction forces are relayed back to the teleoperator for feedback in a 4-Channel PF-PF architecture [13]. Such a method was exploited in [7] to grasp a satellite. This approach, however, does not consider prolonged interactions encountered in an extravehicular tactile inspection task, which requires the fully-actuated (*free-flying*) control of the orbital robot to avoid drifts. Fully-actuated control, however, introduces redundancy, which was exploited in [6] for *in situ* execution of a secondary task, while considering the BTC task as primary. This approach was extended in [14] to provide haptic guidance to the teleoperator about the *in situ* task in a passive way. The approach in [6], [14] is classified as a Partitioned Shared Controller (PSC) [15]. However, [6], [14] assumed a remote robot controller with ideal velocity tracking. Furthermore, to accommodate *free-floating* and *free-flying* functionalities in [6], [14], a blending mechanism for both controllers is required, as shown by [6]. Among *free-flying* regulation works [2], [4], [5], both functionalities were accommodated in [4], i.e., the *free-flying* controller reduced to a *free-floating* approach on the 0-momentum level-set. However, the controller's response to interactions was not analysed. Apart from accommodating functionalities of *both*, *free-flying* and *free-floating* approaches, a stability guarantee during interactions is also required for the controller.

The contributions of this paper are: a) A novel passivity-based *free-flying* PSC for the orbital robot is proposed, which performs a primary interaction-oriented BTC coordination task, e.g. tactile sensing of a telescope, and an *in situ*

All the authors are with the Institute of Robotics and Mechatronics, German Aerospace Center (DLR), Weßling, Germany. e-mail: hrishik.mishra@dlr.de

secondary task for operational safety, e.g. collision avoidance with the telescope. In particular, the BTC is a modified 4-Channel PF-PF architecture because each task occupies a P-channel. b) Asymptotic stability and finite-gain L_2-stability are proved in the absence and presence of interactions, respectively. For static interactions, the PSC is proved to ensure a mechanical equilibrium of the system, i.e., the haptic device and the remote orbital robot. Through this analysis, the *transparency* measure is derived. c) The momentum and shape (joints) dynamics of the orbital robot are exploited in an impedance control design, which avoids the ideal velocity tracking assumption in prior works [6], [14], to obviate acceleration measurements of the haptic device and human-related sensitivity in the spacecraft actuation. d) The proposed *free-flying* approach also offers a *free-floating* functionality on the 0-momentum level-set. e) Furthermore, the proposed PSC is experimentally validated on a hardware-in-the-loop facility. The experiment is shown in the accompanying video.

The paper is organized as follows. The preliminary concepts are introduced in Sec. II. The proposed tasks and error dynamics are derived in Sec. III, and the proposed controller is detailed in Sec. IV. In Sec. V, the experimental validation of this method is summarized. Finally, a discussion and the concluding remarks are provided in Sec. VI.

II. Preliminaries

In this section, the preliminary concepts required for controller development and analysis are described.

A. Motion on the SE(3) Group

Firstly, the relevant details about the motion on the SE(3) group are provided. The pose of a rigid body is a matrix group representation of SE(3) and is written as $g \equiv g(R,p)$, where $R \in \mathrm{SO}(3)$ is the rotation matrix and $p \in \mathbb{R}^3$ is the position. The identity of the SE(3) group is $\mathbb{I}_{4,4}$, where $\mathbb{I}_{k,k}$ is a square identity matrix of dimension k. The tangent and cotangent spaces at $\mathbb{I}_{4,4}$ are denoted as $\mathfrak{se}(3)$ and its dual $\mathfrak{se}(3)^*$, respectively. The spaces $\mathfrak{se}(3)$ and $\mathfrak{se}(3)^*$ are isomorphic to the space of velocity twists and wrenches on $\mathbb{R}^6$ using $(\bullet)^\wedge : \mathbb{R}^6 \to \mathfrak{se}(3), \mathfrak{se}(3)^*$ and $(\bullet)^\vee : \mathfrak{se}(3), \mathfrak{se}(3)^* \to \mathbb{R}^6$, e.g. given a twist, $\mathcal{V} \in \mathbb{R}^6$, $\mathcal{V}^\wedge \in \mathfrak{se}(3)$. The adjoint action of a pose g, $\mathrm{Ad} : \mathfrak{se}(3) \to \mathfrak{se}(3)$, transforms elements of $\mathfrak{se}(3)$ between spatial and body frames, see [16]. The adjoint map of $\mathfrak{se}(3)$ onto itself is, $\mathrm{ad} : \mathfrak{se}(3) \to \mathfrak{se}(3)$, which is the derivative of the Ad map. This is denoted by $\mathrm{ad}_\mathcal{V}$ and its coadjoint map by, $\mathrm{ad}^\top_\mathcal{V} : \mathfrak{se}(3)^* \to \mathfrak{se}(3)^*$. Using this, a skew-symmetric operator, $\mathrm{ad}^\sim_{(\bullet)} : \mathfrak{se}(3) \to \mathfrak{se}(3)^*$, was defined in [17, Def. 4] for the inertia M as, $\mathrm{ad}^\top_v Mw = \mathrm{ad}^\sim_{Mw} v,\ v, w \in \mathbb{R}^6$, and is used here for writing dynamics of the orbital robot. For the details about the introduced quantities, see [17, §2].

The following notations are used in this paper. $\langle a, b\rangle_C = a^\top C b$ given $a, b \in \mathbb{R}^k$, $C \in \mathbb{R}^{k\times k}$. For $A \in \mathbb{R}^{n\times n}$, we indicate $\underline{\sigma}(A)$ ($\overline{\sigma}(A)$) as the lowest (highest, respectively) singular value, $\mathrm{tr}(A)$ as its trace, and $\mathrm{sk}(A)$ as its skew-symmetric part. A is positive-definite if $A \succ 0$. $0_{k,l}$ is a $k \times l$ matrix of zeros, and for $l = 1$, the index is omitted. For ease of notation, the joint position-dependency of dynamic matrices will be given in declaration but will be omitted later.

B. Dynamics of the Haptic Device

In this paper, the haptic device, e.g. a fixed-base manipulator in Fig. 1.**A**, is used to generate the desired SE(3) motion. Its configuration is $\theta \in \mathbb{R}^m$, which is mapped to a pose $g(R,p) \in \mathrm{SE}(3)$ of the end-effector frame $\{\mathcal{E}\}$ relative to an inertial frame $\{\mathcal{I}\}$. Its SE(3) kinematics equation is $\dot{g} = gV^\wedge$, where $V^\wedge \in \mathfrak{se}(3)$ and the manipulator differential kinematics is $V = J(\theta)\dot{\theta}$, where $J(\theta) \in \mathbb{R}^{6\times m}$ is the Jacobian of g. The following assumption is used here.

Assumption 1: The haptic device is non-redundant ($m = 6$) and operates in a singularity-free workspace, i.e. $J \in \mathbb{R}^{6\times 6}$ is invertible. It is also gravity-compensated.

Using Assumption 1, the Cartesian dynamics satisfy,

$$\Lambda(\theta)\dot{V} + \Gamma(\theta,\dot{\theta})V = F + F_h,\ V^\top(\frac{d}{dt}\Lambda - 2\Gamma)V = 0, \quad (1)$$

where $\Lambda, \Gamma \in \mathbb{R}^{6\times 6}$, $F, F_h \in \mathbb{R}^6 \cong \mathfrak{se}(3)^*$ are the matrices of Cartesian inertia ($\Lambda \succ 0$) and the Coriolis/centrifugal (CC) terms, and the wrenches of control (with joint actuation as $\tau_m = J^\top F$) and teleoperator interaction, respectively.

C. Dynamics of the Orbital Robot

The remote orbital robot, see Fig. 1.**B**, is a multibody system consisting of a manipulator with n joints/links mounted on a spacecraft, and its configuration is $x = (g_b, q)$, where $g_b(R_b, p_b) \in \mathrm{SE}(3)$ is the pose of spacecraft frame $\{\mathcal{B}\}$ relative to an inertial frame $\{\hat{\mathcal{I}}\}$ and $q \in \mathbb{R}^n$ denotes the manipulator joint positions. The spacecraft's SE(3) kinematics equation is, $\dot{g}_b = g_b V_b^\wedge$, where $V_b^\wedge \in \mathfrak{se}(3)$.

1) Floating-base Dynamics: The dynamics of the configuration velocity $\nu = \begin{bmatrix} V_b^\top & \dot{q}^\top \end{bmatrix}^\top$ are commonly used as [4],

$$\begin{bmatrix} \Lambda_b(q) & M_{bq}(q) \\ M_{bq}(q)^\top & M_q(q) \end{bmatrix} \begin{bmatrix} \dot{V}_b \\ \ddot{q} \end{bmatrix} + C(q,\dot{q},\dot{V}_b) \begin{bmatrix} V_b \\ \dot{q} \end{bmatrix} = \begin{bmatrix} \mathcal{F}_b \\ \tau_s \end{bmatrix} + \begin{bmatrix} J_b(q)^\top \\ J_e(q)^\top \end{bmatrix} \mathcal{F}_e, \quad (2)$$

where Λ_b, M_{bq}, M_q are the locked, coupling and manipulator inertias, respectively, C is the CC matrix, $\tau_s \in \mathbb{R}^n$ are the joint torques, and $\mathcal{F}_b, \mathcal{F}_e \in \mathbb{R}^6 \cong \mathfrak{se}(3)^*$ are the wrenches of spacecraft actuation and the end-effector interaction, respectively. For the pose $g_e(R_e, p_e) \in \mathrm{SE}(3)$ of end-effector frame $\{\hat{\mathcal{E}}\}$ relative to $\{\hat{\mathcal{I}}\}$, $J_b = \mathrm{Ad}_{g_{be}^{-1}}$ and $J_e \in \mathbb{R}^{6\times n}$ are the spacecraft and manipulator Jacobians, respectively.

Although, the dynamics in (2) are commonly adopted in *free-flying* control design, see e.g. [2], [5], it does not explicitly show the momentum conservation property. This property is pivotal for the *free-flying* controller to also act as a *free-floating* approach on a momentum level-set [4]. To this end, we exploit the momentum and shape (joints) dynamics.

2) Floating-base Dynamics (Momentum and shape): This formulation uses (q, ξ) to describe motion of the orbital robot, where $\xi = \begin{bmatrix} \mu^\top & \dot{q}^\top \end{bmatrix}^\top \in \mathbb{R}^{6+n}$ is a new system velocity with locked velocity, μ, which is defined below.

Def. 1: Locked velocity, μ, is the velocity of the instantaneous equivalent rigid body system, i.e., locked shape (joints) of the orbital robot, and is the velocity corresponding to its total body momentum. It is obtained as $\mu = V_b + \mathcal{A}_l(q)\dot{q}$, where $\mathcal{A}_l = \Lambda_b^{-1} M_{bq}$ is the dynamic coupling factor [3].

Note that a transformation of ν leads to ξ, as $\xi = T(q)\nu$, where $T = \begin{bmatrix} \mathbb{I}_{6,6} & \mathcal{A}_l \\ 0_{n,6} & \mathbb{I}_{n,n} \end{bmatrix}$. Using the transformation (T) of the matrices of inertia and CC terms, the momentum and shape (joints) dynamics are obtained, as in [18, eq. 18]. The structure of the CC terms from this transformation was analysed in detail in [19, Th. 1], which revealed exact velocity dependencies and skew-symmetry that are exploited in this paper. This novel formulation is written as,

$$\begin{bmatrix} \Lambda_b(q) & 0_{6,n} \\ 0_{n,6} & \Lambda_q(q) \end{bmatrix} \begin{bmatrix} \dot{\mu} \\ \ddot{q} \end{bmatrix} + \underbrace{\begin{bmatrix} \frac{1}{2}P(q,\dot{q}) & 0_{6,n} \\ 0_{n,6} & \Gamma_q(q,\dot{q}) \end{bmatrix}}_{\mathcal{D}_{\dot{q}}(q,\dot{q})} \underbrace{\begin{bmatrix} \mu \\ \dot{q} \end{bmatrix}}_{\xi} = \underbrace{\begin{bmatrix} \mathrm{ad}^{\sim}_{\Lambda_b\mu} & -\hat{S}(q,\mu) \\ \hat{S}(q,\mu)^{\top} & -\mathcal{B}(q,\mu) \end{bmatrix}}_{\mathcal{D}_{\mu}(q,\mu)} \begin{bmatrix} \mu \\ \dot{q} \end{bmatrix} + \begin{bmatrix} \mathcal{F}_b \\ \hat{\tau}_s \end{bmatrix} + \begin{bmatrix} J_b(q)^{\top} \\ \tilde{J}_e(q)^{\top} \end{bmatrix} \mathcal{F}_e, \tag{3}$$

where the block-diagonal inertia consists of Λ_b and reduced joint-space inertia, Λ_q [3]. $\mathcal{D}_{\dot{q}}$, $\mathcal{D}_{\mu}$ are the CC matrices, which depend only on $\dot{q}$ and μ, respectively. While Γ_q is the reduced joint-space CC matrix [3], $\hat{S} = \frac{1}{2}S(q,\mu) + \mathrm{ad}^{\sim}_{\Lambda_b\mu}\mathcal{A}_l$ and $\mathcal{B}$ produce CC torques, which are quadratic in μ and cross in $\dot{q}, \mu$ velocities, respectively. In (3), $P(\dot{q}) = \frac{d}{dt}\Lambda_b$ and $S(\mu)^{\top}\mu = \frac{\partial}{\partial q}\langle \mu, \mu \rangle_{\Lambda_b}$, are related to Λ_b. Additionally, $\tilde{J}_e = J_e - J_b\mathcal{A}_l$ is the generalized Jacobian [3] for g_e and $\hat{\tau}_s = \tau_s - \mathcal{A}_l^{\top}\mathcal{F}_b$ is the reduced joint actuation. The dynamics in (3) provide the following property.

Property 1 (Passivity/Skew-symmetry): Given $x \in \mathbb{R}^6$, $y \in \mathbb{R}^n$ and $z = \begin{bmatrix} x^{\top} & y^{\top} \end{bmatrix}^{\top}$, the following holds [19]:

$$x^{\top}\big(\frac{d\Lambda_b}{dt} - P(\dot{q})\big)x = 0,\ y^{\top}\big(\frac{d\Lambda_q}{dt} - 2\Gamma_q(\dot{q})\big)y = 0, \tag{4}$$

$$z^{\top}\mathcal{D}_{\mu}z = 0,\ y^{\top}\mathcal{B}(\mu)y = 0,\ x^{\top}\mathrm{ad}^{\sim}_{\Lambda_b\mu}x = 0. \tag{5}$$

In terms of the new system velocity, ξ, the SE(3) kinematics of the spacecraft and the end-effector are,

$$\dot{g}_b = g_b V_b^{\wedge} = g_b(\mu - \mathcal{A}_l(q)\dot{q})^{\wedge}, \tag{6}$$

$$\dot{g}_e = g_e V_e^{\wedge} = g_e(J_b V_b + J_e\dot{q})^{\wedge} = g_e(J_b\mu + \tilde{J}_e\dot{q})^{\wedge}, \tag{7}$$

where Def. 1 is used to obtain both, (6) and (7).

Therefore, we consider (3) and (6)-(7) to describe the dynamics and kinematics, respectively, of the orbital robot.

D. Passivity in Mechanical Systems

To prove stability of the proposed method during interactions, the concept of L_2-stability is introduced.

Def. 2: Given, state $x \in \mathbb{R}^a$, with input $u \in \mathbb{R}^b$ and output $y \in \mathbb{R}^c$, the dynamical system

$$\dot{x} = f(x,u),\ y = h(x,u) \tag{8}$$

is said to be passive if there exists a continuously differentiable function $V \geq 0$ (storage function), such that $\dot{V} \leq y^{\top}u$. Moreover, it is Output-Strict Passive (OSP) if $\dot{V} \leq -\delta||y||^2 + y^{\top}u,\ \delta > 0$. If (8) satisfies stability, i.e., $f(0,0) = 0_a$, $h(0,0) = 0_c$, and is also OSP, then it is finite-gain L_2-stable and its L_2-gain $\leq \frac{1}{\delta}$ [20], which implies bounded input bounded output for the map $u \mapsto y$.

III. Proposed Tasks and Error Dynamics

In this section, the primary and the secondary tasks are defined for the proposed method, and the resulting error dynamics are derived. For the exposition of our key contributions, a practical on-orbit teleoperation scenario, as in [8], is considered and is stated as the following assumption.

Assumption 2: The human teleoperator is in the proximity of the remote orbital robot, i.e., the detrimental effect of communication time-delays on closed-loop stability is negligible.

A. The Primary BTC Coordination Task

The BTC coordination task requires the tracking of the time-varying end-effector pose of the haptic device with the end-effector pose of the remote orbital robot, i.e., $g_e(t) \to g(t)$. This task is primary because of its positioning accuracy requirements and is achieved using the proposed method as a *free-flying* controller.

The BTC task error, $\eta_e : \mathrm{SE}(3) \times \mathrm{SE}(3) \to \mathrm{SE}(3)$, is defined as $\eta_e = g^{-1}g_e \equiv (\breve{\eta}_e, r_e) = (R^{\top}R_e, R^{\top}(p_e - p))$. The task is formally described by the positive SE(3) potential, $\Phi_e(K_e, \mathcal{K}_e, \eta_e) = \phi(K_e, \breve{\eta}_e) + \frac{1}{2}||r_e||^2_{\mathcal{K}_e}$, where $\phi(\breve{\eta}_e) = \frac{1}{2}\mathrm{tr}\big(K_e(\mathbb{I}_{3,3} - \breve{\eta}_e)\big)$ is the SO(3) potential, and $K_e(\mathcal{K}_e) \in \mathbb{R}^{3\times 3}$ is the rotational (translational) proportional gain matrix. The positive-definiteness of Φ_e is ensured by, firstly, $\mathcal{K}_e \succ 0$, and, secondly, $K_e = \mathrm{diag}(k_{e1}, k_{e2}, k_{e3})$ with $k_{ei} > 0$, where $\mathrm{diag}(\bullet)$ is a diagonal matrix with concatenated arguments. The potential is bounded as $\underline{\Phi}_e < \Phi_e < \overline{\Phi}_e$ due to the boundedness of translational and rotational parts, as shown in [21]. At equilibrium, i.e., $\eta_e = \mathbb{I}_{4,4}$, $\Phi_e = 0$. The time-derivative of Φ_e is obtained, as in [21, eq. (22)], as,

$$\dot{\Phi}_e = \gamma_e(\eta_e)^{\top}(\underbrace{V_e - \mathrm{Ad}^{-1}_{\eta_e}V}_{\delta V}),\ \gamma_e = \begin{bmatrix} \zeta_e(K_e, \breve{\eta}_e) \\ \breve{\eta}_e^{\top}\mathcal{K}_e r_e \end{bmatrix}, \tag{9}$$

where $\zeta_e = [\mathrm{sk}(K_e\breve{\eta}_e)]^{\vee}$, and $\gamma_e \in \mathfrak{se}(3)^* \cong \mathbb{R}^6$ is the proportional wrench corresponding to the error, η_e, and the potential, Φ_e. Note that this choice of η_e, Φ_e ensures that the proportional gains, $K_e, \mathcal{K}_e$, are chosen in the remote orbital robot's end-effector frame, $\{\hat{\mathcal{E}}\}$, which provides an intuitive way to set the desired stiffness towards external interactions.

Using V_e from (7), the velocity error is written as,

$$\delta V = J_b\mu + \tilde{V}_e,\ \tilde{V}_e = \bar{V}_e - \mathrm{Ad}^{-1}_{\eta_e}V, \tag{10}$$

where $\bar{V}_e = \tilde{J}_e\dot{q}$ is the inertial Cartesian velocity of the end-effector due to the shape (joints) velocity, $\dot{q}$. Using δV, the asymptotic stability condition for the BTC task is $\{\eta_e \to \mathbb{I}_{4,4}, \delta V \to 0_6\}$.

Remark 1: To ensure $\delta V \to 0_6$, it is sufficient to ensure both $\mu, \tilde{V}_e \to 0_6$, and this approach is exploited in this paper.

The following assumption is used for the orbital robot.

Assumption 3: The remote orbital robot has a non-redundant manipulator ($n = 6$), which operates in a singularity-free workspace, i.e., $J_e, \tilde{J}_e \in \mathbb{R}^{6\times 6}$ are invertible.

B. The Secondary Task for Automatic Control in situ

Under Assumption 3, the orbital robot has 12 Degrees-of-Freedom (DoF) comprising of the manipulator (6-DoF) and the spacecraft (6-DoF). Of this, only 6-DoF are constrained by the BTC primary task, $\Phi_e(\eta_e)$. Consequently, satisfying $\{\eta_e \to \mathbb{I}_{4,4}, \delta V \to 0_6\}$ alone leaves the remaining DoF unconstrained. During interactions, the motion in the unconstrained DoF might be inimical to the orbital robot's safety, e.g. variation of g_b that tends to a collision with the task structure. Therefore, it is imperative to add a secondary task as a 6-DoF configuration constraint, e.g. spacecraft pose [2]; spacecraft attitude and orbital robot's mass-center [4].

In this paper, the secondary task is defined for a generalized inertial configuration, which is a smooth function of the orbital robot's own configuration as $\mathcal{X} : \mathrm{SE}(3) \times \mathbb{R}^n \to \mathcal{G}$, where $\mathcal{G}$ is a Lie group, e.g. spacecraft pose, $\mathcal{X} = g_b$. This task is a constraint, $\mathcal{X}(x) \in \mathcal{S}$, where $\mathcal{S} \subset \mathcal{G}$ is a time-invariant "safe" space. The task is defined by a positive potential $\Phi_b(\mathcal{X})$, which is bounded, $\underline{\Phi}_b < \Phi_b < \overline{\Phi}_b$, and $\Phi_b = 0$, when $\mathcal{X}(x) \in \mathcal{S}$. The time-derivative of Φ_b takes the form $\dot{\Phi}_b = \gamma_b^\top (T_1(q)V_b + T_2(q)\dot{q})$, where T_1, T_2 are corresponding Jacobians of $\mathcal{X}(x)$ relating to the configuration velocities, ν. Here, $\gamma_b \in \mathbb{R}^6$ is the proportional action required to ensure $\mathcal{X}(x) \in \mathcal{S}$. It is expressed in the basis which is isomorophic to the dual of the algebra in $\mathcal{G}$, i.e., the frames in which $\mathcal{X}$ is defined. Using $\dot{q} = \tilde{J}_e^{-1}\bar{V}$, Def. 1, and $\bar{V}_e$ from the second part of (10), we obtain,

$$\dot{\Phi}_b = \gamma_b^\top \left(T_1\mu + \tilde{T}_2\tilde{J}_e^{-1}\bar{V}_e\right), \tag{11}$$

where $\tilde{T}_2 = (T_2 - T_1\mathcal{A}_l)$. For example, to regulate the spacecraft pose about a setpoint, $g_{bd} \in \mathrm{SE}(3)$, as in [2], $\mathcal{X}(x) = g_b$ and $\mathcal{S} = g_{bd}$. This secondary task error is defined as $\eta_b : \mathrm{SE}(3) \times \mathrm{SE}(3) \to \mathrm{SE}(3)$, $\eta_b = g_{bd}^{-1}g_b$, like the BTC task error. Using (11) with $T_1 = \mathbb{I}_{6,6}$ and $T_2 = 0_{6,n}$, $\dot{\Phi}_b$ is,

$$\dot{\Phi}_b = \gamma_b^\top \left(\mu - \mathcal{A}_l\tilde{J}_e^{-1}(\tilde{V}_e + \mathrm{Ad}_{\eta_e}^{-1}V)\right), \tag{12}$$

where $\gamma_b = \begin{bmatrix} \zeta_b(K_b, \breve{\eta}_b) \\ \breve{\eta}_b^\top \mathcal{K}_b r_b \end{bmatrix}$ is the proportional wrench in the basis which is isomorphic to the dual $\mathfrak{se}(3)^*$, at $\{\mathcal{B}\}$. The terms in (12) assume their interpretations from (9).

C. Orbital Robot's Cartesian Dynamics

The Cartesian dynamics of the orbital robot are the combined dynamics of $\mu, \bar{V}_e$. The dynamics of μ are known from the top row of (3). The dynamics of $\bar{V}_e$ are determined as follows, while exploiting Assumption 3. From $\dot{\bar{V}}_e = \tilde{J}_e\ddot{q} + \dot{\tilde{J}}_e\dot{q}$, $\ddot{q}$ is substituted in the bottom row of (3) and pre-multiplied with $\tilde{J}_e^{-\top}$. Furthermore, replacing $\dot{q} = \tilde{J}_e^{-1}\bar{V}_e$ in the top row of (3), we get the Cartesian dynamics, as,

$$\begin{aligned} &\underbrace{\begin{bmatrix} \Lambda_b & 0_{6,6} \\ 0_{6,6} & \bar{\Lambda}(q) \end{bmatrix}}_{\hat{\Lambda}} \begin{bmatrix} \dot{\mu} \\ \dot{\bar{V}}_e \end{bmatrix} + \underbrace{\begin{bmatrix} \frac{1}{2}P(\bar{V}_e) & 0_{6,6} \\ 0_{6,6} & \bar{\Gamma}(q, \bar{V}_e) \end{bmatrix}}_{\hat{\mathcal{D}}_{\dot{q}}(q, \bar{V}_e)} \begin{bmatrix} \mu \\ \bar{V}_e \end{bmatrix} = \\ &\underbrace{\begin{bmatrix} \mathrm{ad}^{\sim}_{\Lambda_b\mu} & -\bar{S}(q,\mu) \\ \bar{S}(q,\mu)^\top & -\bar{\mathcal{B}}(q,\mu) \end{bmatrix}}_{\hat{\mathcal{D}}_\mu(q,\mu)} \begin{bmatrix} \mu \\ \bar{V}_e \end{bmatrix} + \begin{bmatrix} \mathcal{F}_b \\ \mathcal{F} \end{bmatrix} + \begin{bmatrix} J_b^\top \\ \mathbb{I}_{6,6} \end{bmatrix} \mathcal{F}_e, \end{aligned} \tag{13}$$

where $\bar{\Lambda} = \tilde{J}_e^{-\top}\Lambda_q\tilde{J}_e^{-1}$, $\bar{\Gamma} = \tilde{J}_e^{-\top}(\Gamma_q - \Lambda_q\dot{\tilde{J}}_e)\tilde{J}_e^{-1}$, $\bar{S}^\top = \tilde{J}_e^{-\top}\hat{S}^\top$, $\bar{\mathcal{B}} = \tilde{J}_e^{-\top}\mathcal{B}\tilde{J}_e^{-1}$ and $\mathcal{F} = \tilde{J}_e^{-\top}\hat{\tau}$. The following property is satisfied in (13).

Property 2 (Passivity/Skew-symmetry): Given, any velocity $z = \begin{bmatrix} x^\top & y^\top \end{bmatrix}^\top$ such that $x, y \in \mathbb{R}^6 \cong \mathfrak{se}(3)$, the following holds true:

$$x^\top\left(\frac{d\Lambda_b}{dt} - P(\bar{V}_e)\right)x = 0, \; y^\top\left(\frac{d\bar{\Lambda}}{dt} - 2\bar{\Gamma}(\bar{V}_e)\right)y = 0, \tag{14}$$

$$z^\top\hat{\mathcal{D}}_\mu z = 0. \tag{15}$$

Proof: Skew-symmetry and passivity are invariant to change in velocity coordinates like $\bar{V}_e = \tilde{J}\dot{q}$. Hence, the analogous properties from Property 1 are preserved. ∎

D. BTC Error Dynamics

We recall from Remark 1 that if $\rho = \begin{bmatrix} \mu^\top & \tilde{V}_e^\top \end{bmatrix} \to 0_{12}$, then $\delta V \to 0_6$. To analyse the velocity error (ρ) dynamics, firstly, the dynamics for μ are considered from the top row of (13). Secondly, the dynamics of $\tilde{V}_e$ are simply obtained by differentiating the second part of (10) as,

$$\dot{\tilde{V}}_e = \dot{\bar{V}}_e - \mathrm{Ad}_{\eta_e}^{-1}\dot{V} + \mathrm{ad}_{\delta V}\mathrm{Ad}_{\eta_e}^{-1}V, \tag{16}$$

where the last term is the cross term, which appears due to the time-derivative of the Ad-operator.

For further development, the actuation on *both*, the haptic and the remote agents, are written as a sum of a state-feedback term, ($\tilde{\bullet}$), and a feed-forward action, ($\hat{\bullet}$). This means, for the haptic device, $F = \hat{F} + \tilde{F}$, and for the remote orbital robot, $\mathcal{F} = \hat{\mathcal{F}} + \tilde{\mathcal{F}}$, $\mathcal{F}_b = \hat{\mathcal{F}}_b + \tilde{\mathcal{F}}_b$ corresponding to the manipulator (Cartesian) and the spacecraft actuation, respectively. Therefore, substituting (1) and the bottom row of (13) in (16), $\dot{\tilde{V}}_e$ is written using $\bar{\Lambda}$ as,

$$\begin{aligned} &\bar{\Lambda}\dot{\tilde{V}}_e + \bar{\Gamma}(\bar{V}_e)\bar{V}_e = \bar{S}(\mu)^\top\mu - \bar{\mathcal{B}}(\mu)\bar{V}_e + \hat{\mathcal{F}} + \tilde{\mathcal{F}} + \\ &\mathcal{F}_e - L^{-\top}(-\Gamma V + \hat{F} + \tilde{F} + F_h) + \bar{\Lambda}\mathrm{ad}_{\delta V}\mathrm{Ad}_{\eta_e}^{-1}V, \end{aligned} \tag{17}$$

where $L(q, \theta, \eta_e)^{-\top} = \bar{\Lambda}\mathrm{Ad}_{\eta_e}^{-1}\Lambda^{-1}$ is the dynamically consistent wrench scaling.

It is worth noting that in (17), the actuation terms, $\hat{\mathcal{F}}, \tilde{\mathcal{F}}$ and $\hat{F}, \tilde{F}$, can be chosen to stabilize the $\tilde{V}_e$-dynamics, in a non-unique way. The specific feed-forward choices made in this paper and their reasoning are summarized below.

1) Haptic Device: To ensure *transparency*, i.e., wrench (force) feedback for the teleoperator, a dynamically consistent measure of $\mathcal{F}_e$ is fed to the haptic device as $\hat{F} = L^\top\mathcal{F}_e$.

2) Remote Orbital Robot (Manipulator): Firstly, the dynamically consistent measure of the teleoperator wrench, F_h, is provided as a feed-forward to aid tracking performance. Secondly, instead of cancelling the CC terms in (17), we provide feed-forward of the CC terms so that Property 2 leads to stability. Thirdly, the cross term in R.H.S. of (17) is also compensated. Fourthly, the dynamically scaled CC and actuation torques on the haptic device are also given as a feed-forward. Using these points, from (17), we obtain,

$$\begin{aligned} \hat{\mathcal{F}} =& \left(\bar{\Gamma}(\bar{V}_e) + \bar{\mathcal{B}}(\mu)\right)\mathrm{Ad}_{\eta_e^{-1}}V - \bar{\Lambda}\mathrm{ad}_{\delta V}\mathrm{Ad}_{\eta_e}^{-1}V \\ &+ L^{-\top}F_h + L^{-\top}\left(-\Gamma(V)V + \tilde{F}\right). \end{aligned} \tag{18}$$

3) Remote Orbital Robot (Spacecraft): A feed-forward of $\hat{\mathcal{F}}_b = \bar{S}(\mu)\mathrm{Ad}_{\eta_e}^{-1} V$ compensates the CC terms with $(\mu, \bar{V})$-dependency in the top row of (13).

Substituting the aforementioned choices for $\hat{F}, \hat{\mathcal{F}}, \hat{F}_b$ in (17), we obtain the total error dynamics including the momentum dynamics (top row of (13)) as,

$$\hat{\Lambda}\dot{\rho} + \hat{\mathcal{D}}_{\dot{q}}(\bar{V}_e)\rho = \hat{\mathcal{D}}_{\mu}(\mu)\rho + \begin{bmatrix}\tilde{\mathcal{F}}_b \\ \tilde{\mathcal{F}}\end{bmatrix} + \begin{bmatrix} J_b^\top \\ 0_{6,6}\end{bmatrix}\mathcal{F}_e. \tag{19}$$

Note that (19) has no dependency on the haptic device's end-effector acceleration, which implies a reduced sensory overhead for the BTC, thanks to the decoupled inertia of the momentum and shape dynamics in (3). Another benefit of using (3) is that the tracking performance is achieved by exploiting F_h measurements as feed-forward only through the fast-actuated manipulator, $\hat{\mathcal{F}}$, while avoiding this human-related feed-forward sensitivity in the spacecraft, $\hat{\mathcal{F}}_b$. Additionally, the clear separation of the velocity dependencies in the CC matrices of (3) provides the exact velocity dependency of the CC feed-forward terms in $\hat{\mathcal{F}}, \hat{\mathcal{F}}_b$.

IV. Proposed Partitioned Shared Controller

In this section, the control law is determined based on the following considerations. Firstly, in the absence and presence of external interactions, the controller has to guarantee asymptotic stability of the origin and finite-gain L_2-stability, respectively. For the former, the origin refers to $\eta_e = \mathbb{I}_{4,4}$ and $\delta V = 0_6$ for the BTC error, $V = 0_6$ for the haptic device velocity, and restriction of the orbital robot's configuration to $\mathcal{X}(x) \in \mathcal{S}$. Secondly, on the zero-momentum level-set, i.e $\mu = 0_6$, the PSC should reduce to a *free-floating* controller for the coordination task if the spacecraft actuation is turned off. The following properties from past works are stated here as assumptions and exploited in the stability analysis.

Assumption 4: The human teleoperator defines a passive map (wrench to velocity twist), i.e., $\exists \kappa_h > 0$, $E_h = -\int_0^t V^\top F_h ds + \kappa_h \geq 0$, as in [22].

Assumption 5: The secondary task, as for the typical choices [2], [4], is such that $(T_1 J_b^{-1} - \tilde{T}_2 \tilde{J}_e^{-1})^\top$ is full-rank.

Theorem 1: Given a haptic device and a remote orbital robot, which satisfy Assumptions 1 and 3, and the dynamics of which are described using (1) and (13), respectively, the control law of the proposed PSC below ensures asymptotic stability of the origin, when there are no environmental interactions ($\mathcal{F}_e = 0_6$), and Assumptions 2, 4 and 5 hold.

1) Haptic Device Control Law (Local):

$$F = -D_v V \underbrace{-\mathrm{Ad}_{\eta_e}^{-\top}\tilde{J}_e^{-\top}\tilde{T}_2(q)^\top\gamma_b}_{\text{secondary task}} + \underbrace{\Lambda \mathrm{Ad}_{\eta_e}\bar{\Lambda}^{-1}\mathcal{F}_e}_{\text{wrench feedback}}, \tag{20}$$

which maps to the joint torques as $\tau_m = J(\theta)^\top F$ and $D_v \succ 0$ is the damping gain matrix.

2) Orbital Robot's Spacecraft Control Law (Remote):

$$\begin{aligned}\mathcal{F}_b = &- \underbrace{J_b(q)^\top\big(\gamma_e + D_e\delta V\big) - D_\mu \mu}_{\text{BTC state-feedback}} - \underbrace{T_1(q)^\top\gamma_b}_{\text{secondary task}} \\ &+ \underbrace{\bar{S}(\mu)\mathrm{Ad}_{\eta_e}^{-1}V}_{\text{feed-forward}}.\end{aligned} \tag{21a}$$

3) Orbital Robot's Manipulator Control Law (Remote):

$$\begin{aligned}\mathcal{F} = &\underbrace{\Big(\big(\bar{\Gamma}(\bar{V}_e) + \tilde{\mathcal{B}}(\mu)\big)\mathrm{Ad}_{\eta_e}^{-1} - L^{-\top}(\Gamma(V) + D_v)\Big)V}_{\text{feed-forward}} \\ &- \underbrace{\big(\gamma_e + D_e\delta V + D\tilde{V}_e\big)}_{\text{BTC state-feedback}} \\ &- \underbrace{\bar{\Lambda}\mathrm{ad}_{\delta V}\mathrm{Ad}_{\eta_e}^{-1}V}_{\text{cross-term}} + \underbrace{\bar{\Lambda}\mathrm{Ad}_{\eta_e}^{-1}\Lambda^{-1}F_h}_{\text{wrench feed-forward}} \\ &\underbrace{-\big(L^{-\top}\mathrm{Ad}_{\eta_e}^{-\top} + \mathbb{I}_{6,6}\big)\tilde{J}_e^{-\top}\tilde{T}_2(q)^\top\gamma_b}_{\text{secondary task}},\end{aligned} \tag{21b}$$

which maps to the joint torques as $\tau_s = \tilde{J}_e(q)^\top\mathcal{F} + \mathcal{A}_l(q)^\top\mathcal{F}_b$ and $D_\mu, D, D_e \succ 0$ are the damping gain matrices.

Proof: To use Lyapunov's direct method, the candidate function is chosen as the sum of a kinetic energy-like function of the orbital robot, kinetic energy of haptic device, energy of the human teleoperator and the potentials for the BTC coordination and secondary tasks, as,

$$W = \frac{\langle\mu,\mu\rangle_{\Lambda_b}}{2} + \frac{\langle\tilde{V}_e,\tilde{V}_e\rangle_{\bar{\Lambda}}}{2} + \frac{\langle V,V\rangle_{\Lambda}}{2} + E_h + \Phi_e + \Phi_b. \tag{22}$$

Taking the time-derivative of (22) using (19), (1), Assumption 4, $\dot{\Phi}_e$ from (9) and (10), and $\dot{\Phi}_b$ from (11), we get,

$$\begin{aligned}\dot{W} = &\rho^\top\Big(\big(-\hat{\mathcal{D}}_{\dot{q}}(\bar{V}_e) + \hat{\mathcal{D}}_{\mu}(\mu)\big)\rho + \begin{bmatrix}\tilde{\mathcal{F}}_b \\ \tilde{\mathcal{F}}\end{bmatrix} + \begin{bmatrix} J_b^\top \\ \mathbb{I}_{6,6}\end{bmatrix}\gamma_e \\ &+ \begin{bmatrix} T_1^\top \\ \tilde{J}_e^{-\top}\tilde{T}_2^\top\end{bmatrix}\gamma_b\Big) + V^\top(\tilde{F} + \mathrm{Ad}_{\eta_e}^{-\top}\tilde{J}_e^{-\top}\tilde{T}_2^\top\gamma_b).\end{aligned} \tag{23}$$

Firstly, in (23), $\hat{\mathcal{D}}_{\dot{q}}$ and $\hat{\mathcal{D}}_{\mu}$ satisfy (14) and (15) from Property 2, respectively. It is worth noting that this was possible due to the choice of the feed-forward terms for the orbital robot, $\hat{\mathcal{F}}, \hat{\mathcal{F}}_b$. Secondly, we use the state-feedback terms ($\tilde{\bullet}$) to stabilize the error dynamics as follows. Assigning state-feedback to the haptic device as, $\tilde{F} = -D_v V - \mathrm{Ad}_{\eta_e}^{-\top}\tilde{J}_e^{-\top}\tilde{T}_2(q)^\top\gamma_b$, and together with $\hat{F}$ in (1), we obtain (20). For the remote orbital robot, choosing $\tilde{\mathcal{F}} = -\gamma_e - D_e\delta V - D\tilde{V}_e - \tilde{J}_e^{-\top}\tilde{T}_2^\top\gamma_b$, and together with $\hat{\mathcal{F}}$ we obtain, (21b). For the spacecraft actuation, choosing $\tilde{\mathcal{F}}_b = -J_b^\top\big(\gamma_e + D_e\delta V\big) - D_\mu\mu - T_1^\top\gamma_b$, and together with $\hat{\mathcal{F}}_b$, we get (21a). Substituting the feedback in (23), we get,

$$\begin{aligned}\dot{W} = &-\langle\mu,\mu\rangle_{D_\mu} - \langle\tilde{V}_e,\tilde{V}_e\rangle_{D} - \langle\delta V,\delta V\rangle_{D_e} \\ &- \langle V,V\rangle_{D_v} \leq 0,\end{aligned} \tag{24}$$

which proves the uniform stability of the coordination task error, $(\eta_e, \delta V)$, haptic device velocity V, and the secondary task $\mathcal{X}(x) \in \mathcal{S}$, when $\mathcal{F}_e = 0_6$. Note that, the error dynamics in (19) are rendered time-invariant by the choice of $\hat{F}, \hat{\mathcal{F}}, \hat{\mathcal{F}}_b$. In the level-set $\{\eta_e, \delta V, \mathcal{X}, V : \dot{W} = 0\}$, $\rho, \dot{\rho} = 0_{12}$, i.e.,

$$\begin{bmatrix} J_b & \mathbb{I}_{6,6} \\ T_1 & \tilde{T}_2\tilde{J}_e^{-1}\end{bmatrix}^\top\begin{bmatrix}\gamma_e \\ \gamma_b\end{bmatrix} = 0_{12} \Rightarrow (T_1 J_b^{-1} - \tilde{T}_2\tilde{J}_e^{-1})^\top\gamma_b = 0_6,$$

which means $\gamma_b = 0_6 \Rightarrow \mathcal{X} \in \mathcal{S}$ and $\gamma_e = 0_6 \Rightarrow \eta_e = \mathbb{I}_{4,4}$ under Assumption 5. Hence, using LaSalle's invariance principle, asymptotic stability of $(\eta_e, \delta V, \mathcal{X}, V)$ follows. ■

Lemma 1: The control law in Theorem 1 ensures finite-gain L_2-stability with two OSP mappings, $J_b^\top \mathcal{F}_e \mapsto \mu$ for the orbital robot and, $\left(F_h + L^\top \mathcal{F}_e\right) \mapsto V$ for the haptic device.

Proof: Considering the storage function as $\mathcal{W} = \frac{1}{2}\langle \mu, \mu \rangle_{\Lambda_b} + \frac{1}{2}\langle \tilde{V}_e, \tilde{V}_e \rangle_{\bar{\Lambda}} + \frac{1}{2}\langle V, V \rangle_{\Lambda} + \Phi_e + \Phi_b$, and taking its time-derivative for $\mathcal{F}_e \neq 0_6$ using the same principles from the proof of Theorem 1, we get,

$$\begin{aligned} \dot{\mathcal{W}} \leq & -\underline{\sigma}(D)||\tilde{V}_e||^2 - \underline{\sigma}(D_e)||\delta V||^2 \\ & \underbrace{-\underline{\sigma}(D_\mu)||\mu||^2 + \mu^\top J_b^\top \mathcal{F}_e}_{\text{OSP condition}} \\ & \underbrace{-\underline{\sigma}(D_v)||V||^2 + V^\top (F_h + L^\top \mathcal{F}_e)}_{\text{OSP condition}}. \end{aligned} \tag{25}$$

The proof follows from Def. 2 using Theorem 1 and (25), and it characterizes output (velocities, μ, V) boundedness for interaction-oriented tasks. ■

The BTC in the proposed PSC is a 4-Channel PF-PF architecture, which is composed of a conventional 3-Channel PF-F architecture and an additional P-channel for the secondary task configuration. A block diagram of the proposed method is shown in Fig. 2 with the control law in Theorem 1 emphasized within dashed lines. Its local and remote parts are shown in blue ( ) and yellow ( ) tints, respectively. The 4-Channel PF-PF communication consisting of the pose channels (P-Ch.1 and P-Ch.2) and the wrench channels (F-Ch.1 and F-Ch.2) are highlighted using the red (−) and green (−) nodes, respectively. F-Ch.1 and F-Ch.2 are used to relay the wrench measurements of teleoperator, F_h, and interaction, $\mathcal{F}_e$, respectively. P-Ch.1 is used in the conventional sense for the BTC setpoint, (g, V). In contrast to a conventional BTC [13], P-Ch.2 is used for the secondary task, $\mathcal{X}(x)$.

The *transparency* measure of the BTC in the proposed method is determined using its effective proportional (stiffness) action to a constant interaction wrench as follows.

Lemma 2: The control law in Theorem 1 ensures that the system (haptic device and orbital robot) in the presence of a constant interaction, $\mathcal{F}_e$, has a mechanical equilibrium, i.e., $\mu, \bar{V}_e, V \to 0_6$, which is unique and is defined by,

$$\gamma = \gamma_e + J_b^{-\top} T_1^\top \gamma_b = \mathcal{F}_e, \text{ and } \gamma_e = -\tilde{J}_e^{-\top} \tilde{T}_2^\top \gamma_b, \tag{26a}$$

when the human teleoperator applies a wrench,

$$F_h = -L^\top \mathcal{F}_e + \mathrm{Ad}_{\eta_e}^{-\top} \tilde{J}_e^{-\top} \tilde{T}_2(q)^\top \gamma_b. \tag{26b}$$

Proof: Considering a kinetic-like energy of *both*, the orbital robot and the haptic device,

$$\kappa = \frac{1}{2}\langle \mu, \mu \rangle_{\Lambda_b} + \frac{1}{2}\langle \tilde{V}_e, \tilde{V}_e \rangle_{\bar{\Lambda}} + \frac{1}{2}\langle V, V \rangle_{\Lambda}, \tag{27}$$

as a storage function, and taking its time-derivative while applying the control law from Theorem 1, we obtain,

$$\begin{aligned} \dot{\kappa} = & -\langle \mu, \mu \rangle_{D_\mu} - \langle \tilde{V}_e, \tilde{V}_e \rangle_D - \langle \delta V, \delta V \rangle_{D_e} \\ & + \rho^\top \begin{bmatrix} J_b^\top(-\gamma_e + \mathcal{F}_e) - T_1^\top \gamma_b \\ -\gamma_e - \tilde{J}_e^{-\top} \tilde{T}_2^\top \gamma_b \end{bmatrix} - \langle V, V \rangle_{D_v} \\ & + V^\top (F_h + L^\top \mathcal{F}_e - \mathrm{Ad}_{\eta_e}^{-\top} \tilde{J}_e^{-\top} \tilde{T}_2^\top \gamma_b). \end{aligned} \tag{28}$$

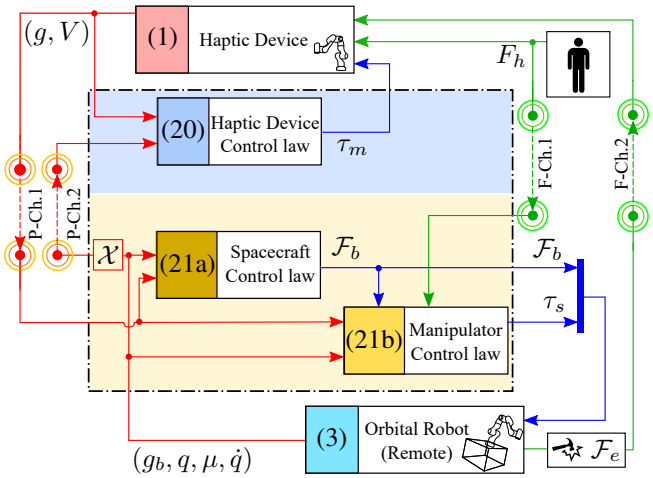

Fig. 2: Block diagram of the Partitioned Shared Controller (PSC, - - -). It is implemented as local ( ) and remote ( ) control laws. In the diagram, → State feedback signals, → Actuation signals and → Interaction wrenches.

Using (26a) and (26b), a level-set is defined for the closed-loop dynamics as, $\Omega = \{(g, V, x, \xi) |$ (26a), (26b)$\}$. Note that (26a) defines a unique equilibrium for γ_e, γ_b, given a constant $\mathcal{F}_e$. Applying the Ω-set conditions, (26a) and (26b), in the sign-indefinite terms of (28), $\kappa \to 0$ because $\dot{\kappa} < 0$, which implies $\mu, \tilde{V}_e, V \to 0_6$. Since $V \to 0_6$, we get $\mu, \bar{V}_e \to 0_6$, which is the system's mechanical equilibrium. ■

Remark 2: In the spirit of [11], (26b) is the static measure of *transparency* for the proposed method. Although the second term on the R.H.S affects the *transparency*, it provides haptic guidance to the teleoperator about the *in situ* secondary task in a manner similar to [14, eq. (7)].

Remark 3: In (26a) and (26b), if $\gamma_b = 0_6$, the mechanical equilibrium is $\mathcal{F}_e = \gamma_e = 0_6$, which implies that κ is non-decreasing in Ω for $\mathcal{F}_e \neq 0_6$. This implies that the secondary task restoring wrench, γ_b, is crucial to ensuring quasi-static interactions, while maintaining a mechanical equilibrium.

Remark 4: A key characteristic of the proposed method in Fig. 2 is that it reduces to a *free-floating* BTC [7] on the 0-momentum level-set, $\mu = 0_6$, if the spacecraft actuation and the secondary task are disabled, i.e., $\gamma_b = 0_6$ and $\mathcal{F}_b = 0_6$.

V. Experimental Validation

The proposed PSC was validated on the OOS-SIM [23] (see Fig. 1), which is a hardware-in-the-loop facility to reproduce the motion of an orbital robot. The manipulators of the remote orbital robot on OOS-SIM (Fig. 1.**B**) and the haptic device (Fig. 1.**A**) are the KUKA-LWR 4+ (locked 3rd joints), the mass and inertia parameters of which are reported in [24, Table 1]. The OOS-SIM's spacecraft parameters were: mass as 700[Kg], and the principal moments of inertia as $(400, 450, 400)$[Kg.m^2]. The remote orbital robot was required to perform a task, which mimics a tactile inspection of the environment with an end-effector sensor. In Fig. 1.**B**, highlighted in red are the Launch Adapter Ring (LAR) profile on the stationary satellite structure and the end-effector gripper tip that acts as the tactile sensor.

The proportional gains for the coordination task were set as $\mathcal{K}_e = 250.\mathbb{I}_{3,3}$[N/m] and $K_e = 40.\mathbb{I}_{3,3}$[N.m/rad.]. The secondary task was spacecraft pose regulation, as in (12), with the proportional gains as $\mathcal{K}_b = 150.\mathbb{I}_{3,3}$[N/m] and $K_b = 20.\mathbb{I}_{3,3}$[N.m/rad.]. The control sequence is summarized in Fig. 3, which consists of: free approach, maintain static contact, and perform sliding contact. In this sequence, only control law from Theorem 1 was used. The end-effectors of the haptic device and the remote orbital robot in Fig. 1 were equipped with force-torque sensors to measure the teleoperator and environment interaction wrenches, respectively.

The results of the experiment are summarized through the plots in Figures 4-8, wherein 1-3 and 4-6 are the translational and rotational bases, respectively. In the plots, the time intervals for static ($t \in [48, 95]$[s]) and sliding ($t \in [120, 145]$[s]) contacts are highlighted using solid and dashed vertical lines, respectively. The tracking performance of the BTC coordination task, i.e., the position errors, r_e, and the orientation errors, $\Delta R = \text{sk}(\breve{\eta}_e).\frac{180}{\pi}$, between the end-effector poses of the orbital robot and the haptic device are shown in Fig. 4.**A**-4.**B**, respectively. The component-wise mean errors for the whole experiment were $(-4.6, -9.1, -3.1)$[mm] and $(-2.2, 2.5, 0.24)[^\circ]$, respectively. The corresponding coordination velocity error (δV) is shown in Fig. 5.**A**, and the locked velocity (μ), which correlates to the momentum of the remote orbital robot, is shown in Fig. 5.**B**. In particular, both δV and μ exhibit a damped response during the contact phases. Notably, after the teleoperator input and interactions cease (last 20[s]), the component-wise means for δV were found to be $(-0.12, 0.01, -0.19)$[mm/s] and $(0.01, -0.01, 0.003)[^\circ/s]$ for the translational and rotational parts, respectively. In the same time interval, the component-wise means for μ were found to be $(-0.14, 0.61, -0.06)$[mm/s] and $(0.09, -0.008, -0.03)[^\circ/s]$ for the translational and rotational parts, respectively.

The measurements of the dynamically consistent teleoperator wrench, $L^{-\top}F_h$, and the negated end-effector interaction wrench, $-\mathcal{F}_e$, are shown in Fig. 6.**A**-6.**B**, respectively. During interactions, $L^{-\top}F_h$ is opposite in sign and approximately equal to $\mathcal{F}_e$, which indicates a high degree of transparency for the teleoperator. The position error, r_b, and the orientation error, $\psi_b(\breve{\eta}_b)$ (123-Euler angles) for the secondary task defined in (12) are shown in Fig. 7.**A**. Note that during interactions, although the secondary task prevents an unbounded drift in the spacecraft pose, it is displaced from its unforced equilibrium exhibiting a compliant behaviour. In Fig. 7.**B**, the spacecraft actuation in the orbital robot's end-effector frame, $\{\hat{\mathcal{E}}\}$, i.e., $J_b^{-\top}\mathcal{F}_b$, is shown. Juxtaposing this with Fig. 6.**B** shows that the spacecraft actuation, $\mathcal{F}_b$, provides the exact stabilizing wrench during interactions, and highlights the *free-flying* functionality of the proposed method. This is evidenced further in Fig. 8 by plotting together the significantly varying bases, $1, 2, 3$, of $-\mathcal{F}_e$ (blue) and $J_b^{-\top}\mathcal{F}_b$ (red). Specifically, the corresponding total proportional action in $J_b^{-\top}\mathcal{F}_b$, i.e., $-\gamma$ (yellow), which is defined in the L.H.S of the first in (26a), is empirically proved to be equal to $-\mathcal{F}_e$ during the interactions. This corroborates the first equality in (26a). Furthermore, from Fig. 6, the equality in (26b) is approximately satisfied while accounting for a negligible contribution from its last term. This contribution is minor because the typical orbital robot considered here has a larger inertia of the spacecraft than that of the manipulator. Thus, Λ_b has a greater contribution

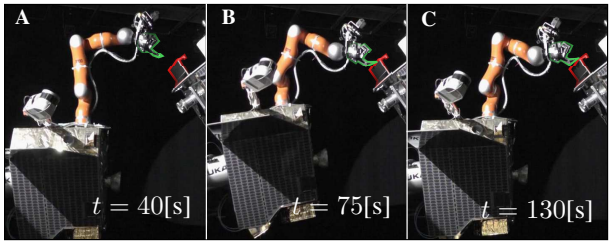

Fig. 3: Control sequence in the experiment (see video attachment). **A**: Approach; **B**: Static contact; **C**: Sliding contact.

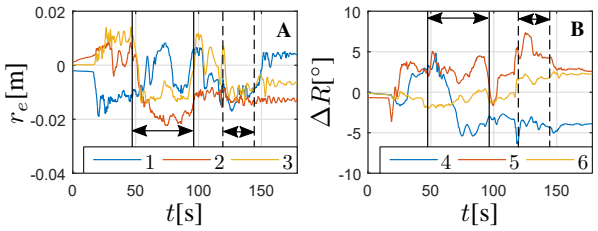

Fig. 4: BTC coordination task error, **A**: position error, r_e; **B**: orientation error, ΔR.

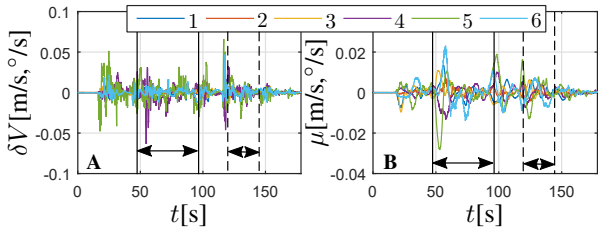

Fig. 5: **A**: BTC velocity error, δV; **B** Locked velocity, μ.

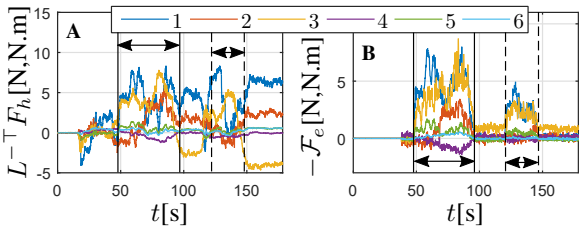

Fig. 6: **A**: Dynamically consistent teleoperator wrench, $L^{-\top}F_h$; **B**: Negated end-effector interaction wrench, $-\mathcal{F}_e$.

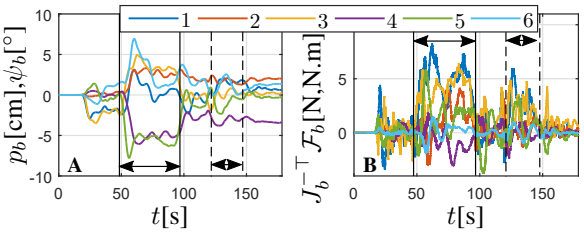

Fig. 7: **A**: Secondary task error, $\eta_b\big(r_b, \psi_b(\breve{\eta}_b)\big)$; **B**: Spacecraft actuation in the orbital robot's end effector frame ($\{\hat{\mathcal{E}}\}$), $J_b^{-\top}\mathcal{F}_b$.

from the former, while M_{bq} depends only on the latter, with $\tilde{T}_2 = -\mathcal{A}_l = \Lambda_b^{-1} M_{bq}$ scaling γ_b weakly in (26b).

Consequently, the experimental validation of Lemma 2 follows from the above inferences of Figures 6 and 8 during the quasi-static interactions. At the end ($t > 150[s]$), the biases in $(r_e, \Delta R)$, (r_b, ψ_b) and F_h in Figures 4, 7.**A** and 6.**A**, respectively, are due to common hardware-in-the-loop modeling errors, e.g. gravity compensation and static friction, which appear as a quasi-static interaction for the proposed method. However, the stability analysis of Lemma 2 holds, and the system equilibrium is given by (26a) and (26b).

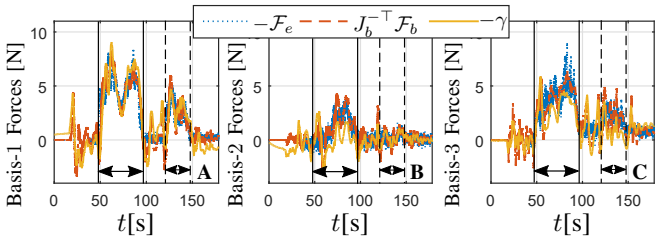

Fig. 8: Forces of interaction ($-\mathcal{F}_e$), spacecraft actuation ($J_b^{-\top}\mathcal{F}_b$), and the total proportional action ($-\gamma$) in the orbital robot's end-effector frame ($\{\hat{\mathcal{E}}\}$) about **A**: Basis-1; **B**: Basis-2; and **C**: Basis-3.

VI. Discussion and Conclusion

A novel partitioned shared controller was proposed in Theorem 1, which performed a primary interaction-oriented end-effector task using a remote bilateral teleoperation controller, while the secondary task was automatically controlled *in situ* for operational safety. The decoupled inertia and well-defined Coriolis/centrifugal matrices in the momentum and shape (joints) dynamics of the orbital robot were exploited to benefit controller design in reducing sensory overhead and avoiding human-related feed-forward sensitivity in the spacecraft actuation. In the absence of interactions, asymptotic stability was proved for the proposed method. The method's suitability for interactions was proved through finite-gain L_2-stability and mechanical equilibrium analysis in Lemmas 1-2. Finally, the method was experimentally validated on an on-ground hardware-in-the-loop simulator through an experiment requiring static and sliding contacts.

The proposed method offers the functionalities of *both*, *free-flying* and *free-floating* control approaches. In particular, by simply disabling the spacecraft actuation and the secondary task on the 0-momentum level-set, it simplifies to a *free-floating* approach, as noted in Remark 4. It is also worth differentiating the proposed method's attributes from typical bilateral teleoperation applications [13]. Firstly, the states of *both*, the coordination task and the secondary task are exchanged over the two position (pose) channels. Secondly, the *transparency* measure was shown to consist of wrench feedback of not just the remote interaction, but also the secondary task, as stated in Remark 2. Thirdly, the secondary task was shown to be crucial for stable interactions while executing the primary teleoperation task, as stated in Remark 3. For the sake of clarity, Assumption 2 was used. If, however, the time-delay is non-negligible, as in bilateral teleoperation from an on-ground station, a passivity-based method [7] can be employed, and this is our future work.

References

[1] A. Flores-Abad *et al.*, "A review of space robotics technologies for on-orbit servicing," *Progress in Aerospace Sciences*, vol. 68, 2014.

[2] E. Papadopoulos and S. Dubowsky, "Coordinated manipulator/spacecraft motion control for space robotic systems," in *IEEE International Conference on Robotics and Automation (ICRA)*, pp. 1696–1701 vol.2, 1991.

[3] K. Yoshida and D. N. Nenchev, "A general formulation of under-actuated manipulator systems," in *Robotics Research*, (London), pp. 33–44, Springer London, 1998.

[4] A. M. Giordano *et al.*, "Workspace fixation for free-floating space robot operations," in *IEEE International Conference on Robotics and Automation (ICRA)*, pp. 889–896, 2018.

[5] M. De Stefano *et al.*, "Multi-rate tracking control for a space robot on a controlled satellite: A passivity-based strategy," *IEEE Robotics and Automation Letters*, vol. 4, pp. 1319–1326, April 2019.

[6] J. R. Spofford and D. L. Akin, "Redundancy control of a free-flying telerobot," *Journal of Guidance, Control, and Dynamics*, vol. 13, no. 3, pp. 515–523, 1990.

[7] J. Artigas *et al.*, "Teleoperation for on-orbit servicing missions through the ASTRA geostationary satellite," in *IEEE Aerospace Conference (AEROCONF)*, pp. 1–12, 2016.

[8] C. Parrish, "The ranger telerobotic shuttle experiment: An on-orbit satellite servicer," in *Artificial Intelligence, Robotics and Automation in Space*, vol. 440, p. 225, 1999.

[9] T. Imaida *et al.*, "Ground-space bilateral teleoperation of ETS-VII robot arm by direct bilateral coupling under 7-s time delay condition," *IEEE Transactions on Robotics and Automation*, vol. 20, no. 3, pp. 499–511, 2004.

[10] G. Hirzinger *et al.*, "ROKVISS-robotics component verification on ISS," in *Proc. 8th International Symposium on Artificial Intelligence, Robotics and Automation in Space (iSAIRAS) p. Session2B*, 2005.

[11] Y. Yokokohji and T. Yoshikawa, "Bilateral control of master-slave manipulators for ideal kinesthetic coupling-formulation and experiment," *IEEE Transactions on Robotics and Automation*, vol. 10, no. 5, pp. 605–620, 1994.

[12] P. F. Hokayem and M. W. Spong, "Bilateral teleoperation: An historical survey," *Automatica*, vol. 42, no. 12, pp. 2035–2057, 2006.

[13] D. Lawrence, "Stability and transparency in bilateral teleoperation," *IEEE Transactions on Robotics and Automation*, vol. 9, no. 5, pp. 624–637, 1993.

[14] M. Selvaggio *et al.*, "Passive task-prioritized shared-control teleoperation with haptic guidance," in *International Conference on Robotics and Automation (ICRA)*, pp. 430–436, 2019.

[15] T. Inagaki *et al.*, "Adaptive automation: Sharing and trading of control," *Handbook of cognitive task design*, vol. 8, pp. 147–169, 2003.

[16] F. Bullo and R. Murray, "Tracking for fully actuated mechanical systems: a geometric framework," *Automatica*, vol. 35, no. 1, pp. 17–34, 1999.

[17] H. Mishra *et al.*, "A nonlinear observer for free-floating target motion using only pose measurements," in *American Control Conference (ACC)*, pp. 1114–1121, Jul 2019.

[18] G. Garofalo *et al.*, "On the inertially decoupled structure of the floating base robot dynamics," *IFAC-PapersOnLine, International Conference on Mathematical Modelling*, vol. 48, no. 1, pp. 322 – 327, 2015.

[19] H. Mishra *et al.*, "On the dynamics of floating-base robots: Linking the recursive formulation to the Reduced Euler-Lagrange Equations," Sep 2020. Preprint doi: 10.13140/RG.2.2.28765.84961/1.

[20] H. K. Khalil, *Nonlinear systems (3rd edition)*. Upper Saddle River, NJ: Prentice-Hall, 2002.

[21] H. Mishra *et al.*, "A geometric controller for fully-actuated robotic capture of a tumbling target," in *American Control Conference (ACC)*, pp. 2150–2157, 2020.

[22] E. Nuño, L. Basañez, and R. Ortega, "Passivity-based control for bilateral teleoperation: A tutorial," *Automatica*, vol. 47, no. 3, 2011.

[23] J. Artigas *et al.*, "The OOS-SIM: An on-ground simulation facility for on-orbit servicing robotic operations," in *IEEE International Conference on Robotics and Automation (ICRA)*, May 2015.

[24] M. De Stefano *et al.*, "An energy-based approach for the multi-rate control of a manipulator on an actuated base," in *IEEE International Conference on Robotics and Automation (ICRA)*, pp. 1072–1077, May 2018.